Above-band-gap dielectric functions of ZnGeAs$_2$: Ellipsometric measurements and quasiparticle self-consistent GW calculations

S. G. Choi,[1,*] M. van Schilfgaarde,[2] D. E. Aspnes,[3] A. G. Norman,[1] J. M. Olson,[1] T. J. Peshek,[1,2,†] and D. H. Levi[1]

[1]*National Renewable Energy Laboratory, Golden, Colorado 80401, USA*

[2]*School for Engineering of Matter, Transport and Energy, Arizona State University, Tempe, Arizona 85287, USA*

[3]*Department of Physics, North Carolina State University, Raleigh, North Carolina 27695, USA*

We report the above-band-gap dielectric-function spectra $\varepsilon_a = \varepsilon_{a1} + i\varepsilon_{a2}$ of single-crystal ZnGeAs$_2$ grown epitaxially on (001)GaAs, and study it theoretically. After surface overlayers were removed chemically to minimize artifacts, pseudodielectric-function spectra $\langle \varepsilon \rangle = \langle \varepsilon_1 \rangle + i\langle \varepsilon_2 \rangle$ were acquired ellipsometrically from 1.5 to 6.0 eV with the sample at room temperature. The ε_a spectra were then extracted by multilayer analysis. The procedure ensures that the result is a close approximation to the a-axis component of the dielectric-function tensor $\varepsilon = \varepsilon_1 + i\varepsilon_2$ of ZnGeAs$_2$. The data exhibit numerous spectral features associated with critical points. The energies of these critical points are determined accurately by fitting standard line shapes to second energy derivatives of the data obtained by a combined method of spectral analysis. We compare our results to the predictions of quasiparticle self-consistent GW calculations. Good agreement is achieved for the major critical-point features, and their probable origins are identified.

I. INTRODUCTION

The II-IV-V$_2$ chalcopyrite-phase ternary compound ZnGeAs$_2$ is the logical extension of the III-V binary compound GaAs, where the Zn and Ge reside at adjacent Ga sites in an ordered manner.[1] Because its 1.15-eV band gap is direct and its *in-plane* lattice parameter is close to that of (001)GaAs, ZnGeAs$_2$ layers can be incorporated into the conventional Ga$_{0.52}$In$_{0.48}$P/GaAs/Ge three-junction solar-cell structure to allow more efficient capture of incoming photons without compromising lattice structure. As a result, ZnGeAs$_2$ is a promising constituent for high-efficiency III-V-multijunction solar cells.[2,3] In addition, a newly proposed tandem-cell concept[4] based on ZnGeAs$_2$ and related II-IV-V$_2$ compounds is revitalizing interest in this material.

Knowledge of the optical response of solids, for example the dielectric function $\varepsilon = \varepsilon_1 + i\varepsilon_2$ and refractive index $N = n + ik = \sqrt{\varepsilon}$, is necessary for the design and development of high-performance photonic and photovoltaic devices.[5] Even though a limited number of reflectance spectra of ZnGeAs$_2$ are available,[6–10] ε and N data are rare. The ε spectra reported in Ref. 10 were calculated indirectly by a Kramers-Kronig (K-K) transform of low-temperature (80 K) reflectance data of polycrystalline ZnGeAs$_2$. The results are therefore a mix of the two components of the dielectric-function tensor of this optically uniaxial material. In addition, it is well known[11] that K-K analysis of reflectance data may lead to systematic errors, so an independent determination is justified.

To obtain our data we use spectroscopic ellipsometry (SE). SE is a nondestructive optical technique[11] that can determine ε and N accurately over a wide range of photon energies without need of K-K analysis. As a result, SE has been widely used to study optical properties of many semiconductors in the past few decades.[12] Our data concern the intrinsic ε of a ZnGeAs$_2$ thin film grown epitaxially on GaAs. Since ZnGeAs$_2$ grows with its c axis normal to the surface and SE measurements are dominated by the component(s) of the ε tensor perpendicular

to the c axis (here parallel to the measurement surface),[13,14] our data are a close approximation to the component ε_a of ε. This is the component relevant for normal-incidence illumination. We compare our data to the predictions of quasiparticle self-consistent GW calculations.[15] We also report accurate values of the critical-point (CP) energies, which we determine using a combined method of spectral analysis.[16] Finally, we use the approximate self-consistent electronic-structure method to identify the probable origins of the CP features.

II. EXPERIMENT

A 200-nm film of chalcopyrite-phase ZnGeAs$_2$ was grown epitaxially on a lattice-matched Ga$_{0.52}$In$_{0.48}$P buffer layer on a 6° B-miscut GaAs(001) substrate by low-pressure (50 Torr) metalorganic vapor-phase epitaxy. The nominal thickness of the Ga$_{0.52}$In$_{0.48}$P buffer layer was 250 nm. The sources were arsine, germane, and diethylzinc. Chalcopyrite ZnGeAs$_2$ grows only under a very narrow range of conditions.[17] More generally, body-centered tetragonal Zn$_3$As$_2$ forms instead, which is lattice mismatched to GaAs and hence contains a high density of dislocations.

We confirmed the chalcopyrite phase with transmission electron diffraction (TED) using a Philips CM30 transmission electron microscope (TEM) operating at 300 kV. The pattern shown in Fig. 1(a) was obtained from a plan-view TEM sample of the ZnGeAs$_2$ layer, tilted to what would be the [111] pole for the zinc blende structure. The arrow indicates the array of extra spots that do not occur for zinc blende material, but which are in excellent agreement with the calculated pattern for the [111] pole of chalcopyrite ZnGeAs$_2$. Energy dispersive x-ray microanalysis (EDX) data (not shown) verify the presence of Zn, Ge, and As at the expected ratios within experimental uncertainty. Additionally, the [110] high-resolution cross-section TEM image given in Fig. 1(b) shows a defect-free interface between epitaxial ZnGeAs$_2$ and Ga$_{0.52}$In$_{0.48}$P as well as the high crystalline quality of ZnGeAs$_2$ film.
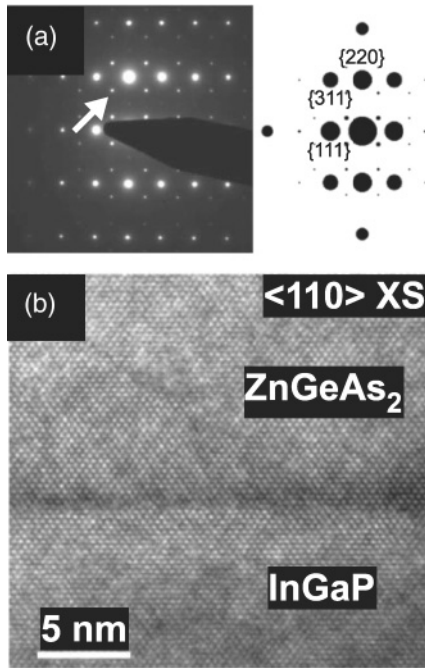
FIG. 1. (a) TED pattern taken at the [112] zinc blende zone axis of the ZnGeAs$_2$. By comparison to the calculated pattern on the right for chalcopyrite ZnGeAs$_2$ ([111] zone axis for this structure), the extra spots indicated by the arrow show that chalcopyritephase ZnGeAs$_2$ has been grown. (b) High-resolution cross-sectional TEM image of a ZnGeAs$_2$ layer grown epitaxially on In$_{0.48}$Ga$_{0.52}$P on (001)GaAs.

SE data were acquired from 1.5 to 6.0 eV using an automatic spectroscopic rotating-compensator ellipsometer operating at an angle of incidence of 67.08°. The polarizer and analyzer azimuths were both set to 30°, and a 504-μm-thick MgF$_2$ monoplate was used as the compensator. The sample was optically prealigned and maintained in a windowless cell under flowing purified N$_2$. This unique configuration[18] enabled us to chemically strip the surface overlayers while monitoring the effectiveness of the cleaning procedure in real time. Our sequence consisted of de-ionized (DI) water, methanol, a 50 vol% solution of NH$_4$OH in DI water (AmH) followed by DI water rinse, and a 0.01 vol% solution of Br in methanol (BrM) followed by a methanol rinse. Chemical treatments were repeated until the SE data showed no further changes, which is indicative of a flat surface with a minimal overlayer.[18]

Effects of chemical treatments on the $\langle \varepsilon_2 \rangle$ spectrum of ZnGeAs$_2$ are shown in Fig. 2(a). The significant increase in the value of $\langle \varepsilon_2 \rangle$ in the 4–5 eV range indicates the removal of a fairly thick surface overlayer[19] in accordance with previous studies.[18,20] The effect of the initial DI water rinse [not shown in Fig. 2(a)] is strongly positive, suggesting that a major component of the surface overlayer is a Ge-related oxide. Oxides related to As were removed by AmH, and Zn-related oxides and other residues (including microscopic roughness) were removed by BrM.[18]

A side benefit of these treatments is that several optical structures are better resolved. Structure in the spectral range below ∼2 eV is slightly blue shifted after exposure to BrM, which suggests that the associated features are due to
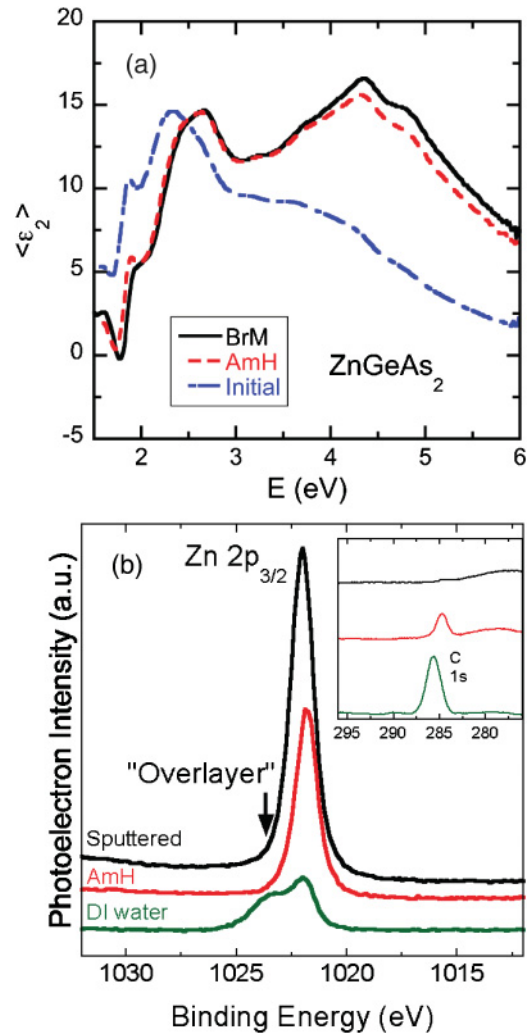

FIG. 2. (Color online) (a) Effects of chemical treatments on $\langle \varepsilon_2 \rangle$ for ZnGeAs$_2$. Note that the optical structure is better resolved in the data for the treated sample. (b) XPS spectra of Zn 2$p_{3/2}$ peak for ZnGeAs$_2$ acquired for different surface preparations: DI water rinse (solid green line), AmH (a 50 vol% solution of NH$_4$OH in DI water) rinse (solid red line), and *in situ* Ar sputter cleaned (solid black line). For clarity, the data with AmH treatment and Ar sputtering are offset upward. Inset: XPS spectra showing the C 1s peak. The reduction of C-related contamination is clearly seen after AmH treatment.

interference, and that BrM removes not only overlayers but also the top few layers of ZnGeAs$_2$.

The positive effects of the AmH treatment were confirmed by x-ray photoemission spectroscopy (XPS). Figure 2(b) shows XPS spectra acquired in a Physical Electronics 5600 photoemission system using monochromatic Al Kα radiation, a 45° take-off angle, and an 800-μm slit. The pass energy was 29.35 eV and the dwell time per data point was 2 s. Compared to the XPS data for surface rinsed with DI water (solid green line, "DI water"), those for the AmH-treated surface (solid red line, "AmH") show a significant enhancement of the Zn 2$p_{3/2}$ peak intensity at 1022 eV as well as the disappearance of the "overlayer" peak. This demonstrates the effectiveness of the AmH treatment. As shown in the inset of Fig. 2(b), AmH
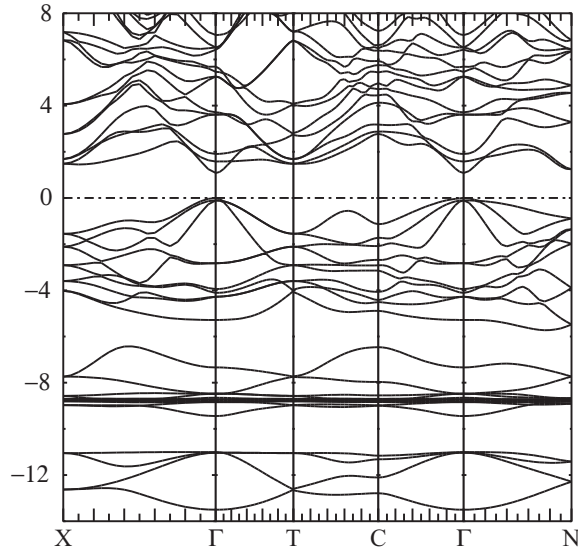
FIG. 3. Electronic energy-band structure of ZnGeAs$_2$ calculated in the QS*GW* approximation. The k-point labels T and N correspond to X and L in the zinc blende structure.

treatment also reduces the amount of C-related contaminants on the ZnGeAs$_2$ surface.

As a reference, the XPS spectrum for the surface prepared by *in situ* Ar sputtering (solid black line) is included in Fig. 2(b). Here, the surface was processed by a 1-keV Ar$^+$ beam with a current density of 6 μA/cm^2. Even though the AmH treatment does not fully compete with *in situ* sputter cleaning, it eliminates a major fraction of surface contamination. In fact, sputtering can lead to phase segregation in addition to causing near-surface damage, which potentially adversely affects the optical data.[11] Therefore, the *in situ* wet-etching procedures described here enabled us to minimize overlayer artifacts and hence to obtain a close approximation to the intrinsic optical functions of ZnGeAs$_2$.

III. QUASIPARTICLE SELF-CONSISTENT *GW* (QS*GW*) CALCULATIONS

The electronic energy-band structure of ZnGeAs$_2$ calculated within the QS*GW* approximation[15] is presented in Fig. 3. The ε spectra along the two principal axes a and c were also calculated within the random phase approximation (RPA)[21] and compared to the SE data, to be discussed in Sec. IV. The local density approximation (LDA) to density functional theory (DFT) has been widely used for these purposes, but the LDA-DFT approach tends to underestimate semiconductor band gaps ("LDA gap error") and describes conduction-band dispersion poorly.

The QS*GW* approximation used in this study is a new first-principles method of solving the Schrödinger equation within Hedin's *GW* theory.[22] This approach essentially uses the low-order terms in many-body perturbation theory. Because it is an expansion about a noninteracting Hamiltonian H_0, the calculated band structure depends strongly on the choice of H_0. Standard implementations of *GW* use the LDA to construct H_0. However, this procedure suffers from underestimating

semiconductor band gaps, and the amount of underestimation varies from one semiconductor to another. In the QS*GW*, self-consistency is used to select a H_0 as close as possible to the full interacting Hamiltonian H. The QS*GW* is an internally consistent scheme that no longer depends on the LDA.

The QS*GW* approximation is highly reliable, and is sufficiently accurate to predict key properties over a wide range of materials systems. Even though small errors occur, these are systematic and understandable. In the present context, the predominant error arises from the RPA used in the ε calculations. Electron-hole excitations in the virtual states are included only in the time-dependent Hartree approximation (also known as RPA), leaving out the contributions from the attractive interactions. Therefore, the peaks in the ε_2 spectrum appear at energies higher than those observed. As can be seen from the K-K relations connecting ε_1 and ε_2, this error results in a systematic underestimation of ε_∞. This leads in turn to a slight overestimation of the $W(\omega \rightarrow 0)$ that is the predominant contribution to the *GW* self-energy, since it scales as $1/\varepsilon_\infty$. As a consequence, the band-gap energies are overestimated by $\sim$0.2–0.3 eV for many III-V semiconductors.[21]

In principle, we can reduce the above problems by including the electron-hole attraction in the calculations through the ladder diagram,[23] although this procedure is costly in practice. Given that ε_∞ is systematically overestimated by a universal factor of 0.8, a simple solution is to scale $\Sigma = iGW$ by 0.8.[21] With this correction, the band-gap energies for many semiconductors and insulators are described very accurately with a gap error typically <0.1 eV.

The QS*GW* gap for ZnGeAs$_2$ is estimated to be 1.3 eV, but the scaling procedure described above reduced it to 1.1 eV. Although the differences are relatively small, we present the band structure with the scaled Σ to obtain a band structure that is as accurate as possible.

IV. RESULTS AND DISCUSSION

Our best ZnGeAs$_2$ $\langle \varepsilon \rangle$ data, shown in Fig. 2(a), were further analyzed by a multilayer model consisting of the ambient, a surface-roughness layer, the ZnGeAs$_2$ layer, the Ga$_{0.52}$In$_{0.48}$P buffer layer, and the GaAs substrate as shown in the inset of Fig. 4. Because the c-axis contribution is minor, we ignore the anisotropic nature of ZnGeAs$_2$. We analyzed the $\langle \varepsilon \rangle$ data by using the known optical functions of bulk Ga$_{0.52}$In$_{0.48}$P and GaAs[18] and representing the ZnGeAs$_2$ spectrum with nine Gaussian oscillators. We estimated the surface-roughness layer to be $\sim$0.25 nm thick, and modeled its response as a Bruggeman effective-medium-approximation (BEMA)[24,25] 50-50 mixture of the ZnGeAs$_2$ layer and void. The ellipsometric data Ψ and Δ, and their best-fit curves are shown as the open symbols and solid lines, respectively, in Fig. 4. Model and data are in excellent agreement. Only 20% of the actual data points are presented here to show clearly the quality of fit.

The ε data that we obtained are given in Table I. The spectra themselves are shown in Fig. 5(a), along with ε spectra calculated for the polarization field perpendicular (ε_a) and parallel (ε_c) to the c axis. The SE results are given as solid lines, and the calculations for ε_a and ε_c as dotted and dashed lines, respectively. By comparing Figs. 2(a) and 5(a), we see that
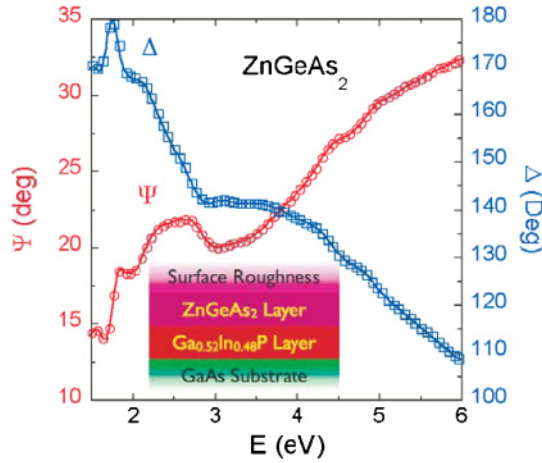
FIG. 4. (Color online) Data (open symbols) and the best-fit curves (solid lines) for Ψ and Δ of ZnGeAs$_2$. Only 20% of the data points are presented to show clearly the quality of fit. Inset: The structure used in the multilayer model.

most spectral features are preserved whereas the interference oscillations below 2 eV are eliminated.

As seen in Fig. 5(a), ZnGeAs$_2$ exhibits many CP features, more than its III-V counterpart, GaAs. This is partly due to the difference in atomic structure. Since the Brillouin-zone (BZ) volume of chalcopyrite is four times smaller than that of zinc blende, there is a 4-to-1 mapping of energy levels of the zinc blende BZ into the chalcopyrite BZ.[1] As a result, the energy

TABLE I. Dielectric function $\varepsilon = \varepsilon_1 + i\varepsilon_2$ of ZnGeAs$_2$ obtained by modeling as described in the text.

| E (eV)	ε_1	ε_2	E (eV)	ε_1	ε_2
1.5	15.130	2.135	4.1	5.741	16.283
1.6	15.536	2.336	4.2	4.695	16.854
1.7	16.075	2.558	4.3	3.241	17.195
1.8	16.863	2.857	4.4	1.650	16.954
1.9	18.010	3.576	4.5	0.431	16.217
2.0	18.898	5.001	4.6	−0.268	15.508
2.1	19.616	6.523	4.7	−0.869	15.149
2.2	20.090	8.977	4.8	−1.774	14.826
2.3	19.138	11.726	4.9	−2.753	14.115
2.4	17.162	13.578	5.0	−3.392	13.157
2.5	15.131	14.458	5.1	−3.727	12.296
2.6	13.233	14.905	5.2	−3.974	11.581
2.7	11.234	14.776	5.3	−4.200	10.922
2.8	9.713	13.766	5.4	−4.384	10.280
2.9	9.285	12.586	5.5	−4.513	9.661
3.0	9.491	12.058	5.6	−4.587	9.074
3.1	9.604	12.097	5.7	−4.617	8.530
3.2	9.493	12.263	5.8	−4.613	8.030
3.3	9.353	12.414	5.9	−4.588	7.574
3.4	9.275	12.649	6.0	−4.550	7.159
3.5	9.186	13.058			
3.6	8.968	13.627			
3.7	8.550	14.260			
3.8	7.949	14.849			
3.9	7.246	15.340			
4.0	6.522	15.778			
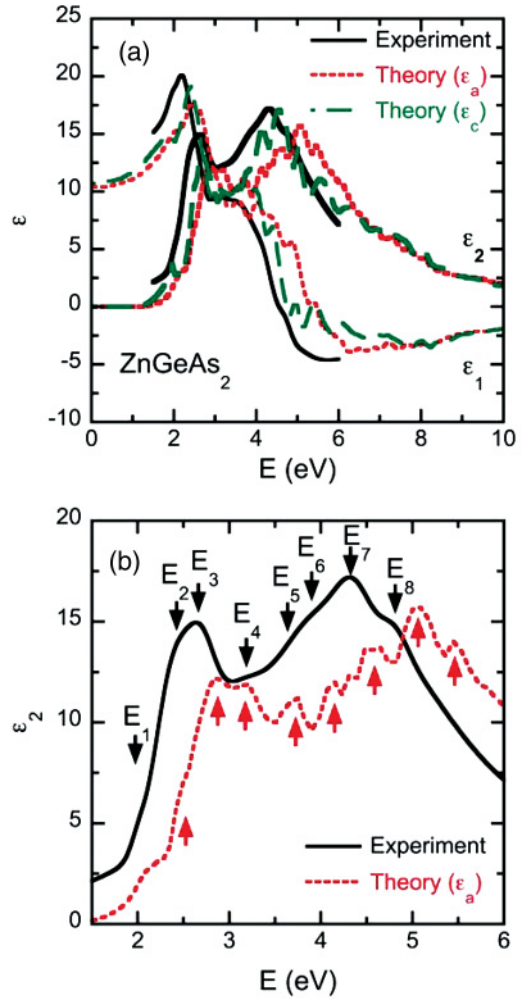
FIG. 5. (Color online) (a) Ellipsometric data ε_1 and ε_2 (solid black lines) compared to ε_a (dotted red lines) and ε_c (dashed green lines) calculated in the QSGW approximation. (b) Detailed comparison between ε_2 and the calculated ε_{a2} spectrum from 1.5 to 6.0 eV. Eight critical-point structures are identified and are indicated by arrows. A systematic difference of $\sim$0.5 eV occurs between the CP energies determined from the data and those obtained by calculation due to the simplicity of the calculation.

band structure and related optical functions of chalcopyrite crystals are complicated. In addition, the selection rules are somewhat relaxed for the lower symmetry. Thus, some of the transitions that are forbidden in GaAs are allowed for ZnGeAs$_2$.[7]

The agreement between the data and calculated ε_a spectrum is reasonable. All the pronounced CP structures observed in ε_2 are identified in the QSGW results, as indicated in Fig. 5(b) by the arrows. The difference of $\sim$0.5 eV in the CP energies between data and calculation is expected, since the RPA calculations consider the electron-hole interactions in the virtual excitations whereas the data actually contain many-body effects. The second discrepancy is that the calculations underestimate the magnitude of ε_2 in the region below $\sim$4 eV and overestimate it above $\sim$5 eV. Discrepancies in the predicted energies and amplitudes of CP struc-tures are commonly seen in these calculations.[26] Despite

these differences, the peaks in the QS*GW* spectrum accurately reflect the splittings in the quasiparticle (QP) levels, i.e., the differences between unoccupied and occupied states. The good agreement between the SE-determined ε data and the calculated ε_a spectrum also validates the argument that the SE-determined ε data are a good approximation to the ordinary component ε_a of the dielectric tensor for ZnGeAs$_2$.

To obtain energies of the CP structures observed in Fig. 5, we used a newly developed combined method of spectral analysis.[16] First, we Fourier transformed the *pseudodielectric-function* $\langle\varepsilon_1\rangle$ and $\langle\varepsilon_2\rangle$ data, shown in Fig. 2, to generate the reciprocal-space (RS) coefficients $C_n e^{i\xi_n}$, where C_n and ξ_n are the amplitude and phase, respectively, of the *n*th coefficient.[27] The advantage in doing this is that base line, information, and noise are separated in the $C_n e^{i\xi_n}$. These coefficients were then filtered with a high-index Gaussian cutoff. The direct-space second-derivative spectra were then reconstructed from these filtered coefficients. Use of the second derivative is advantageous for two reasons. First, it provides the filtering needed to suppress base-line effects. Second, its construction requires most of the intermediate-index coefficients, and hence it makes highly efficient use of CP information. Standard CP expressions were then least-squares fit to the reconstructed derivatives. These standard expressions are[28,29]

$$\frac{d^2\varepsilon}{dE^2} = \begin{cases} n(n-1)Ae^{i\phi}(E - E_g + i\Gamma)^{n-2}, & n \neq 0 \\ Ae^{i\phi}(E - E_g + i\Gamma)^{-2}, & n = 0 \end{cases}, \quad (1)$$

where A is the amplitude, E_g is the threshold energy, Γ is the broadening parameter, and ϕ is the excitonic-phase angle. For $A > 0$, the values $n = -1, -1/2, 0$, and $1/2$ represent excitonic, one-, two-, and three-dimensional line shapes, respectively. Both real and imaginary parts were fit simultaneously.

The open circles and squares in Fig. 6 represent the reconstructed $d^2\langle\varepsilon_1\rangle/dE^2$ and $d^2\langle\varepsilon_2\rangle/dE^2$ spectra, respectively. For clarity, the number of data points (symbols) was reduced by half. The solid and dash-dotted lines are the best-fit curves to the real and imaginary parts, respectively, using the excitonic line shape $n = -1$. A total of eight CP line shapes were
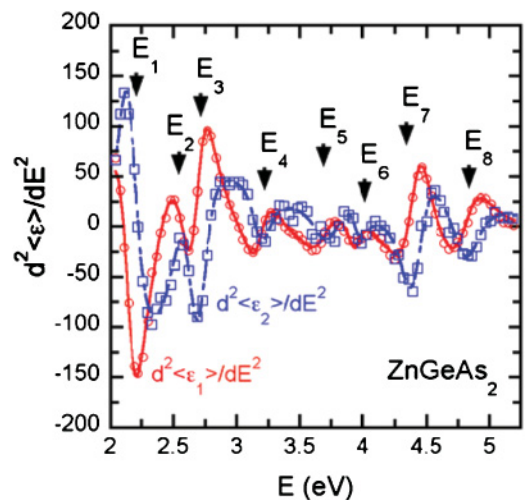

FIG. 6. (Color online) Red and blue solid lines: standard CP line shapes best fit to second energy derivatives $d^2\langle\varepsilon_1\rangle/dE^2$ (open circles) and $d^2\langle\varepsilon_2\rangle/dE^2$ (open squares), respectively, where $d^2\langle\varepsilon_1\rangle/dE^2$ and $d^2\langle\varepsilon_2\rangle/dE^2$ are calculated as described in the text. For clarity, only half the data points are shown. Energies of each CP are indicated by arrows and labeled following Ref. 7.

needed to analyze the spectrum from 2 to 5.25 eV. The CP energies obtained are listed in Table II. The labeling follows that of a previous room-temperature reflectance study.[7] For comparison, the CP energies[6–10,30] previously reported are also included.

To understand the origin of each CP structure, we calculated several ε_2 spectra, resolving the contributions from particular valence bands using the approximate self-consistent electronic-structure method. Zinc blende GaAs has four valence bands when spin-orbit coupling is not included. In principle, chalcopyrite ZnGeAs$_2$ has 16 valence bands because it has four times more atoms per unit cell than GaAs. In addition, two of these atoms are Zn, which have $3d$ states. These add another ten bands. Therefore, we considered a system consisting of 52 electrons in a total of 26 bands for our

TABLE II. CP energies in eV for ZnGeAs$_2$. Suggested valence- and conduction-band origins for each CP are also listed. For example, the E_4 CP is attributed to transitions from the 16th valence band to the third and fourth conduction bands. Previously reported CP energies are also included for comparison.

| CP		E_1	E_2	E_3	E_4	E_5	E_6	E_7	E_8
This work	Expt.	2.15 ± 0.01	2.53 ± 0.05	2.68 ± 0.02	3.19 ± 0.02	3.70 ± 0.05	3.94 ± 0.03	4.42 ± 0.01	4.82 ± 0.02
	Calc.	2.53	2.88	3.18	3.73	4.15	4.59 $13^{VB} \rightarrow 1,2^{CB}$	5.06 $12^{VB} \rightarrow 2^{CB}$	5.46 $11^{VB} \rightarrow 1,2^{CB}$
			$15,16^{VB} \rightarrow 1,2^{CB}$		$16^{VB} \rightarrow 3,4^{CB}$	$14^{VB} \rightarrow 1,2^{CB}$	$15^{VB} \rightarrow 3^{CB}$	$14^{VB} \rightarrow 3,4^{CB}$	$15^{VB} \rightarrow 5^{CB}$
Ref. 7		2.34	2.50	2.82	3.23	3.76	4.05	4.43	4.80
Ref. 8		2.27	2.43	2.72	3.24, 3.40	3.75	4.07	4.40	
Ref. 10		2.39	2.55	2.68, 2.85	3.10, 3.36	3.60	3.89, 4.17	4.51	4.83
Ref. 9			2.46	2.70	3.24, 3.46		3.80	4.50	4.92
Ref. 6		2.26	2.41	2.74, 2.92	3.23	3.80		4.37	4.92
Ref. 30		2.35	2.42, 2.50	2.68	3.03, 3.30	3.61, 3.68	4.05, 4.22	4.45	
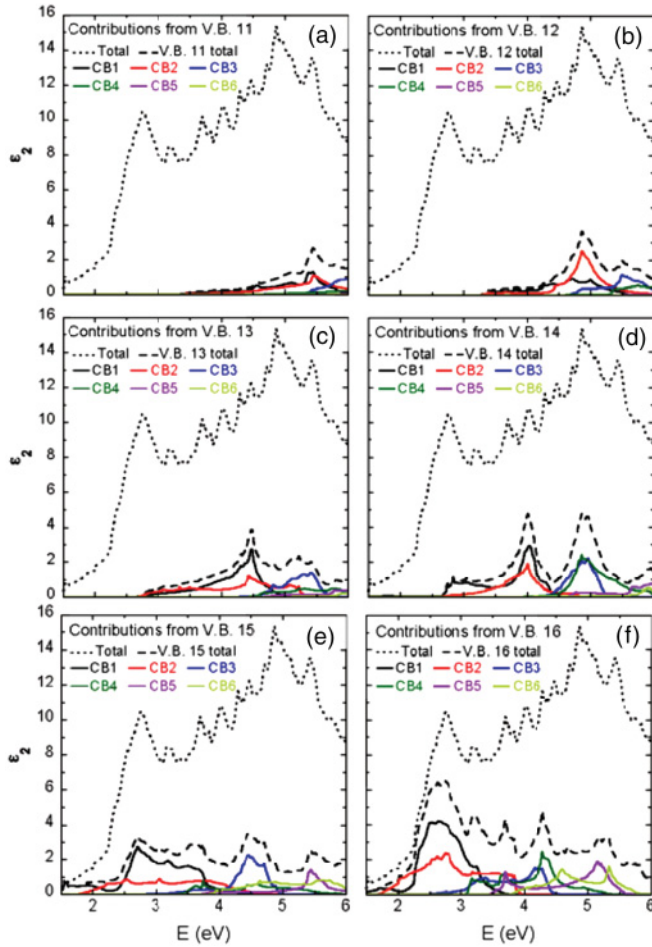
FIG. 7. (Color online) (a)–(f) Contributions to ε_2 from the 11th through the uppermost 16th valence bands, respectively, calculated in the self-consistent electronic-structure approximation. The dashed lines show the total contributions from the specific valence bands, for comparison to the overall total shown as the dotted lines. Contributions from the specific valence bands to individual conduction bands are shown as the colored solid lines. Note: The total dielectric-function spectrum (dotted curve) appears slightly different from the one shown in Fig. 5, which stems from the difference in the calculation method. The dielectric functions are calculated more accurately by the QS*GW* approximation (Fig. 5) while the contributions from individual valence band-to-conduction band transitions are better resolved by the self-consistent electronic-structure approximation.

calculations. However, the additional ten $3d$ bands are very deep and reside $\sim$8–9 eV below the valence-band maximum. To make the comparison with GaAs simpler, we conceptually regarded them as the core bands and assigned number 16 to the uppermost valence band. Figures 7(a)–7(f) show the ε_2 spectra

resulting from the individual valence bands 11 through 16 to separate conduction bands (solid colored lines), then to all available conduction bands (dashed lines).

For zinc blende semiconductors the dominant CP features are due to transitions localized at or near high-symmetric points of the BZ, such as Γ, L, and X. The corresponding locations for the chalcopyrite structures are Γ, N, and T (see Fig. 3). The E_1, E_2, and E_3 CPs of ZnGeAs$_2$ shown in Fig. 5 are analogous to the E_1 and $E_1 + \Delta_1$ CPs for GaAs, and occur in the vicinity of the N points.[8] Figures 7(e) and 7(f) suggest that these CP structures are primarily due to transitions from the 15th and 16th valence bands to the first and second conduction bands. The E_4 CP of ZnGeAs$_2$ does not have a GaAs counterpart, and this structure has been attributed to the transitions along the F line between the Γ and N points.[8] Transitions from the 16th valence band to the third and fourth conduction bands are responsible for this CP structure, as suggested in Fig. 7(f). The higher-energy CPs of ZnGeAs$_2$ are analogous to the E_0' and E_2 CPs of GaAs, and seem to have multiple contributions as revealed in Fig. 7. The major contributions to each CP structure are summarized in Table II.

V. CONCLUSION

SE has been used to determine the component ε_a of the dielectric-function tensor of chalcopyrite ZnGeAs$_2$, where ε_a is the component of ε perpendicular to the c axis. We used *in situ* wet chemical etching to obtain $\langle\varepsilon\rangle$ data least affected by surface overlayers and then obtained ε spectrum using the multilayer analysis, which is thus most closely related to ε_a. Our $\langle\varepsilon\rangle$ data exhibit eight CP structures from 2 to 5.25 eV, and their energies are obtained accurately by the combined method of spectral analysis. The data show good agreement with the ε_a spectrum calculated in the quasiparticle self-consistent *GW* approximation. In addition, we calculated ε_a using the approximate method of self-consistent electronic structure to obtain the separate contributions of the uppermost six valence bands, so that we can better elucidate possible origins of these features.

[*]sukgeun.choi@nrel.gov

[†]Present address: eQED, LLC, Mayfield Village, Ohio 44143, USA.

[1]U. Kaufmann and J. Schneider, in *Advances in Solid State Physics*, edited by H. J. Queisser (Pergamon, Oxford, 1974) Chap. 14.

[2]S. R. Kurtz, D. Myers, and J. M. Olson, in *Proceedings of the 26th IEEE Photovoltaics Specialist Conference* (IEEE, New York, 1997), p. 875.

[3]A. Janotti, S.-H. Wei, S. B. Zhang, and S. Kurtz, Phys. Rev. B **63**, 195210 (2001).

[4]M. van Schilfgaarde, T. J. Coutts, N. Newman, and T. Peshek, Appl. Phys. Lett. **96**, 143503 (2010).

[5]M. Law, M. C. Beard, S. Choi, J. M. Luther, M. C. Hanna, and A. J. Nozik, Nano Lett. **8**, 3904 (2008).

[6]C. C. Y. Kwan and J. C. Woolley, Can. J. Phys. **48**, 2085 (1970).

[7]V. I. Donetskich, A. S. Poplavnoi, and V. V. Sobolev, Phys. Status Solidi B **48**, 541 (1971).

[8]G. Z. Krivaite and A. Yu. Shileika, Sov. Phys. Semicond. **7**, 1198 (1974).

[9]J. C. Rife, R. N. Dexter, P. M. Bridenbaugh, and B. W. Veal, Phys. Rev. B **16**, 4491 (1977).

[10]V. V. Sobolev, V. E. Grachev, and S. P. Batanov, J. Appl. Spectrosc. **63**, 221 (1996).

[11]D. E. Aspnes, in *Handbook of Optical Constants of Solids*, edited by E. D. Palik (Academic, Orlando, FL, 1985), Vol. I, p. 89.

[12]S. Adachi, *Optical Constants of Crystalline and Amorphous Semiconductors: Numerical Data and Graphical Information* (Kluwer, Boston, 1999).

[13]D. E. Aspnes, J. Opt. Soc. Am. **70**, 1275 (1980).

[14]G. E. Jellison Jr. and J. S. Baba, J. Opt. Soc. Am. A **23**, 468 (2006).

[15]S. V. Faleev, M. van Schilfgaarde, and T. Kotani, Phys. Rev. Lett. **93**, 126406 (2004).

[16]S. G. Choi, D. E. Aspnes, N. A. Stoute, Y. D. Kim, H. J. Kim, Y.-C. Chang, and C. J. Palmstrøm, Phys. Status Solidi A **205**, 884 (2008).

[17]G. S. Solomon, M. L. Timmons, and J. B. Posthill, J. Appl. Phys. **65**, 1952 (1989).

[18]D. E. Aspnes and A. A. Studna, Phys. Rev. B **27**, 985 (1983).

[19]Multilayer analysis, discussed in Sec. IV, suggests that $\sim$9.5 nm of oxide (modeled as GeO_2) was removed by the chemical treatment.

[20]Y.-D. Kim, S. L. Cooper, M. V. Klein, and B. T. Jonker, Appl. Phys. Lett. **62**, 2387 (1993).

[21]M. van Schilfgaarde, T. Kotani, and S. Faleev, Phys. Rev. Lett. **96**, 226402 (2006).

[22]L. Hedin, Phys. Rev. **139**, A796 (1965).

[23]M. Shishkin, M. Marsman, and G. Kresse, Phys. Rev Lett. **99**, 246403 (2007).

[24]D. E. Aspnes, Thin Solid Films **89**, 249 (1982).

[25]G. E. Jellison Jr., L. A. Boatner, D. H. Lowndes, R. A. McKee, and M. Godbole, Appl. Opt. **33**, 6053 (1994).

[26]M. Rohlfing and S. G. Louie, Phys. Rev. B **62**, 4927 (2000).

[27]S. D. Yoo and D. E. Aspnes, J. Appl. Phys. **89**, 8183 (2001).

[28]M. Cardona, *Modulation Spectroscopy, Solid State Physics, Suppl. 11*, edited by F. Seitz, D. Turnbell, and H. Ehrenreich (Academic, New York, 1969).

[29]D. E. Aspnes, in *Handbook of Semiconductors*, edited by M. Balkanski (North-Holland, Amsterdam, 1980), Vol. 2, p. 109.

[30]N. A. Zakharov and V. A. Chaldyshev, Sov. Phys. Semicond. **16**, 763 (1982).